

Cite this: *J. Mater. Chem. A*, 2019, 7, 11520

# Realization of ultra-long columnar single crystals in TiO<sub>2</sub> nanotube arrays as fast electron transport channels for high efficiency dye-sensitized solar cells†

Nianqing Fu,<sup>ab</sup> Yandong Duan,<sup>c</sup> Wei Lu,<sup>b</sup> Mingshan Zhu,<sup>cd</sup> Guoge Zhang,<sup>a</sup> Dongmei Xie,<sup>c</sup> Yuan Lin,<sup>c</sup> Mingdeng Wei<sup>de</sup> and Haitao Huang<sup>ab</sup>

A balance between strong light-harvesting and efficient charge collection is not only important but also challenging for photoelectrochemical applications. We developed here TiO<sub>2</sub> nanotube arrays (TNTAs) with ultra-long single crystals on the nanotube walls and along the axial direction. Those oriented nanotubes show ultra-fast 1D electron transport due to the reduction of grain boundaries that scatter electrons. Based on the TNTAs with ultra-long crystals, we further developed an electronically heterogeneous hierarchical architecture for dye-sensitized solar cell (DSSC) application. In this crafted structure, the columnar single crystals on the nanotube walls provide well-aligned pathways with high electron mobility for rapid electron transport, while a mesoporous TiO<sub>2</sub> network welded on the nanotube walls provides sufficient surface area for dye loading. The significant mismatch in electron mobility between the TNTA scaffold and mesoporous TiO<sub>2</sub> network drains the electrons from the TiO<sub>2</sub> network to the TNTAs, enabling high charge collection efficiency exceeding 90% within a ~30 μm film. As a result, an impressively high power conversion efficiency (PEC) exceeding 10% was achieved for the resulting DSSCs with such a TNTA based hierarchical structure. The presented technology provides a promising prospect for constructing multi-hierarchical structures for a wide range of applications, such as photocatalysis, batteries and gas sensors.

Received 8th January 2019  
Accepted 3rd April 2019

DOI: 10.1039/c9ta00241c

rsc.li/materials-a

## 1. Introduction

In the past few decades, dye-sensitized solar cells (DSSCs) have attracted tremendous interest as a low-cost and versatile solar energy conversion technology. The power conversion efficiency (PCE) of DSSCs has so far reached a value of 14.3% under 100 mW cm<sup>-2</sup> illumination (using cocktail organic dyes of ADEKA-1 and LEG4)<sup>1</sup> and 32% under indoor light with low intensity (1000 lux).<sup>2</sup> Besides the counter electrode and electrolyte,<sup>3-8</sup> the photoanode is another key component of DSSCs that determines the device performance. A classic DSSC consists of a dye

anchored TiO<sub>2</sub> photoanode in which the TiO<sub>2</sub> scaffold acts as an electron acceptor and transports the photo-generated electrons toward the collecting electrode. Therefore, a vast surface area for dye loading and an unhindered pathway for fast electron transport are the most favorable properties for a photoanode of DSSCs to maximize light harvesting and minimize recombination.<sup>9-11</sup> The most straightforward approach to increase the surface area is increasing the photoactive film thickness. However, the improved light harvesting is commonly offset by increased recombination loss due to the limited electron diffusion length in a thick film with plenty of grain boundaries.<sup>9-12</sup> Constructing hierarchical architectures, which combine high surface area nanoparticles with fast 1D electron transport channels, is regarded as a promising approach to meet the aforementioned requirements and address the problems encountered by the photoanodes using a 1D structure (fast electron transport but a limited surface area) or NPs alone (high surface area but low electron transport in random pathways).<sup>9-28</sup> A most frequently investigated hierarchical structure is the combination of anodized 1D TiO<sub>2</sub> nanotube arrays (TNTAs) and small TiO<sub>2</sub> NPs.<sup>9-11,28-32</sup> However, the efficiency of these TNTA hybrid based devices is commonly inferior to that of NP based solar cells because the obtained hybrid architectures still do not

<sup>a</sup>School of Materials Science and Engineering, South China University of Technology, Guangzhou 510640, P. R. China

<sup>b</sup>Department of Applied Physics, The Hong Kong Polytechnic University, Hong Kong, P. R. China. E-mail: aphhuang@polyu.edu.hk

<sup>c</sup>Beijing National Laboratory for Molecular Sciences, Key Laboratory of Photochemistry, Institute of Chemistry, Chinese Academy of Sciences, Beijing 100190, P. R. China

<sup>d</sup>School of Environment, Jinan University, Guangzhou 510632, P. R. China. E-mail: mingshanzhu@yahoo.com

<sup>e</sup>Institute of Advanced Energy Materials, Fuzhou University, Fuzhou, Fujian 350002, P. R. China

† Electronic supplementary information (ESI) available. See DOI: 10.1039/c9ta00241c

fully meet the requirements of an ideal structure: (1) fast enough electron transport within the TNTA itself, (2) a large enough surface area available for dye adsorption and (3) a good enough electrical mismatch between the fast electron transport pathways and the large surface dye molecule anchoring sites, as sketched in Scheme 1.

It is reported that TNTA based DSSCs did not show remarkably superior electron transport to NP based devices, because the nanotube (derived from the ethylene glycol (EG) electrolyte) walls are composed of polycrystalline  $\text{TiO}_2$  anatase with a similar small grain size (tens of nanometers) to NPs.<sup>33</sup> The electron mobilities in  $\text{TiO}_2$  bulk single crystals ( $20 \text{ cm}^2 \text{ V}^{-1} \text{ s}^{-1}$ ) and thin films ( $4 \text{ cm}^2 \text{ V}^{-1} \text{ s}^{-1}$ ) are significantly higher than that in  $\text{TiO}_2$  NP films ( $0.034 \text{ cm}^2 \text{ V}^{-1} \text{ s}^{-1}$ ).<sup>24,34–36</sup> There is plenty of room for improvement in the electron transport within TNTAs and thus the charge collection efficiency (*i.e.* enhanced electron transport together with suppressed charge recombination) if a DSSC is built using TNTAs composed of single or large and well-oriented anatase crystals. Schmuki's recent work introduced a nanotwinned grain structure within the  $\text{TiO}_2$  nanotubes, which provides enhanced electron transport and the resulting DSSC gained an efficiency of >10%.<sup>37</sup> More importantly, due to the electrically homogeneous nature (similar electron mobility and conductivity) of the small particle based TNTAs and the decorated  $\text{TiO}_2$  NPs, competitive electron transport pathways (within TNTAs and NP decorated layers) were observed in hierarchical hybrids with multiple layers of granular  $\text{TiO}_2$  (Scheme 1b),<sup>30</sup> where the photo-generated electrons can be effectively drained to the TNTAs only when the decorated nanoparticles are isolated or form a single layer. In this regard, formation of hierarchical structures with enough electrical heterogeneity is crucial to drive the electron transfer from low conductivity NP decorations into high conductivity TNTAs and to enable the device with substantially fast electron transport and thus high charge collection efficiency (Scheme 1a). Unfortunately, the as-anodized amorphous NTNAs derived

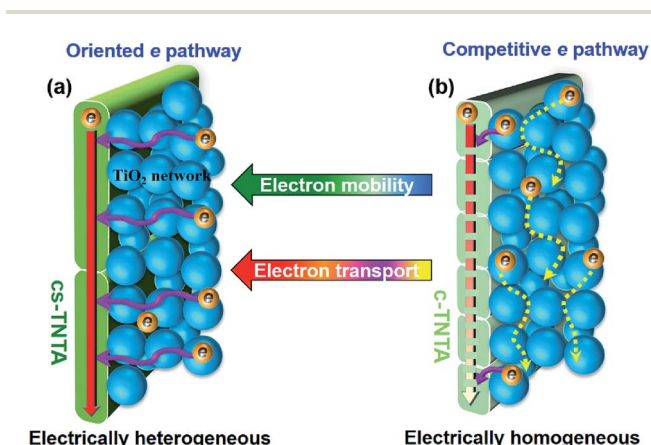
from an EG electrolyte are prone to convert into polycrystalline nanotubes consisting of small nanoparticles after post-annealing,<sup>38–40</sup> which makes the fabrication of single-crystal or larger-crystal based TNTAs a great challenge.

The  $\text{TiO}_2$  NPs/TNTA hybrid structure is typically achieved by  $\text{TiCl}_4$  hydrolysis treatment or chemical/water bath soaking.<sup>28–32</sup> However, the thin particulate layers (20–30 nm in thickness with an individual particle size of  $\sim 5$  nm) attached on the nanotube wall can only improve the specific surface area by a small amount and the improvement in cell efficiency is thus limited. Schmuki's group developed a layer-by-layer modified  $\text{TiO}_2$ -NPs/TNTA hybrid architecture by repetitive  $\text{TiCl}_4$  treatment several times and an efficiency of around 8% was achieved for the back-side illuminated DSSCs, which suggests that increasing the thickness of the decorated  $\text{TiO}_2$  layer is a promising approach to boost the light harvesting and thus the solar cell efficiency.<sup>9</sup>

In this work, well-aligned TNTAs consisting of large columnar single crystals were developed by controlled anodization. Following a novel vacuum-assisted  $\text{TiO}_2$  sol-filling approach, a "cigar-like"  $\text{TiO}_2$  NP-network/TNTA hybrid architecture was obtained. The mesoporous  $\text{TiO}_2$  network enables about 3.8 times the dye-loading amount of the pristine TNTA electrode. More importantly, this hybrid structure shows remarkable electrical heterogeneity between columnar single-crystal based TNTAs and  $\text{TiO}_2$  NP decorations, which favors unhindered oriented electron transfer from  $\text{TiO}_2$  networks into TNTAs and provides a significantly high charge collection efficiency of over 90% in the thick photoactive film ( $\sim 30 \mu\text{m}$ ). The resulting DSSCs yield a power conversion efficiency of 10.1%, which is even better than that of nanoparticle based cells (9.62%).

## 2. Results and discussion

The classic  $\text{TiO}_2$  nanotube arrays (denoted as c-TNTAs) derived from a typical EG/fluoride electrolyte have a double layer structure, as claimed in earlier reports,<sup>9,22</sup> and illustrated in Fig. S1a.† The TEM image displayed in Fig. 1a reveals a coarse appearance of c-TNTA walls. The abundant grain boundaries of small crystals (average crystallite size about 30 nm) will slow down the charge transport due to electron scattering, as schematically shown in Scheme 1b. To obtain larger grains in TNTAs, the electrolyte for anodization was modified by employing DMSO as a co-solvent with a carefully controlled  $\text{H}_2\text{O}$  content. The SEM image of the TNTAs (denoted as cs-TNTAs) formed in the novel electrolyte composed of EG-DMSO (50/50 vol%) with 0.4 wt%  $\text{NH}_4\text{F}$  and 1.8 vol%  $\text{H}_2\text{O}$  demonstrates a single-walled nanotube morphology (Fig. S1b†). The TEM image shown in Fig. 1b illustrates clearly the single-walled nanotubes built from well-aligned large columnar crystals. The average length of the columnar crystals as determined from the low resolution TEM image is about 235 nm (Fig. S2†), which is much larger than the wall thickness and roughly ten times the grain size of c-TNTAs. The interlayer spacing of 0.351 nm (Fig. 1d) can be assigned to the *d*-spacing of (101) crystal planes of anatase  $\text{TiO}_2$  while the selected-area electron diffraction



**Scheme 1** Illustration of electron transport in (a) the electrically heterogeneous hierarchical  $\text{TiO}_2$ -network/cs-TNTA architecture with an oriented electron pathway and in (b) the electrically homogeneous hierarchical  $\text{TiO}_2$ -network/c-TNTA architecture with a competitive electron transport pathway, showing the electron-draining effect of long columnar crystal based TNTAs with high electron mobility.

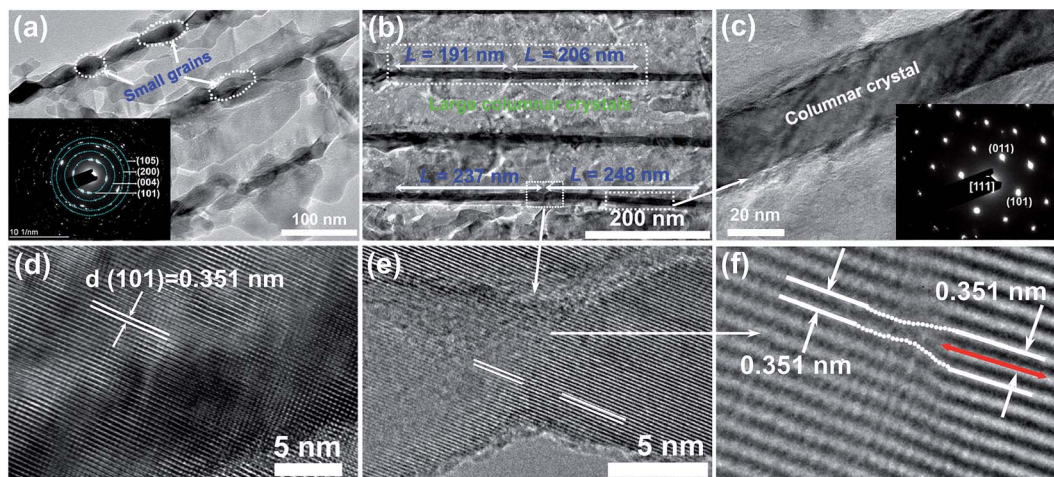


**Fig. 1** Morphological details of the classical and newly developed  $\text{TiO}_2$  nanotube array. TEM images of the classical TNTAs derived from (a) a conventional EG electrolyte system and (b) the newly developed EG/DMSO electrolyte system. (c and d) HRTEM images and SAED pattern (inset of c) of the TNTAs from the EG/DMSO electrolyte. (e) HRTEM image of TNTAs from the EG/DMSO electrolyte, focusing on the junction of two seemingly columnar crystals. (f) Enlarged HRTEM image of (e) at the junction part, showing the existence of a stacking fault.

(SAED) pattern (inset of Fig. 1c) indicates the single crystalline nature of the large columnar crystals. It should be noted that the crystal length as determined from low-resolution TEM images (Fig. S2<sup>†</sup>) is actually under-estimated. The HRTEM image (Fig. 1e) focusing on the junction part of two seemingly columnar single crystals demonstrates the same well-aligned parallel (101) crystal planes across the junction part, indicating that the two crystals displayed in the low-resolution TEM image (Fig. 2b) are actually one. A stacking fault is clearly observed at the junction part (Fig. 1f, S3<sup>†</sup>). In contrast, the c-TNTAs consist of randomly arranged small particles with mismatched grain boundaries (Fig. S4<sup>†</sup>). X-ray diffraction patterns shown in Fig. S5<sup>†</sup> reveal the anatase feature of both samples, while the cs-TNTAs exhibit much stronger and sharper diffraction peaks than c-TNTAs, indicating larger grains in cs-TNTAs, which is in line with the TEM observation. One can reasonably speculate that

the large grain size of the long columnar single crystals of cs-TNTAs will facilitate much faster oriented electron transport along the axial direction of nanotubes than in the case of c-TNTAs where the large number of grain boundaries impede the electron diffusion by scattering. More importantly, larger grains are commonly associated with higher electron mobility,<sup>24,34–36</sup> providing a possibility to construct electrically heterogeneous architectures with  $\text{TiO}_2$  NPs.

The solvent and  $\text{H}_2\text{O}$  content in anodizing solution play key roles in growth dynamics and thus the composition and crystalline nature of the as-anodized TNTAs, which will significantly alter the morphology of the obtained TNTAs after annealing. It is demonstrated that the inclusion of DMSO into the electrolyte can suppress the formation of a carbon (which is derived from EG oxidation products) enriched inner shell to form “single-walled”  $\text{TiO}_2$  nanotubes, since the DMSO was more efficient in

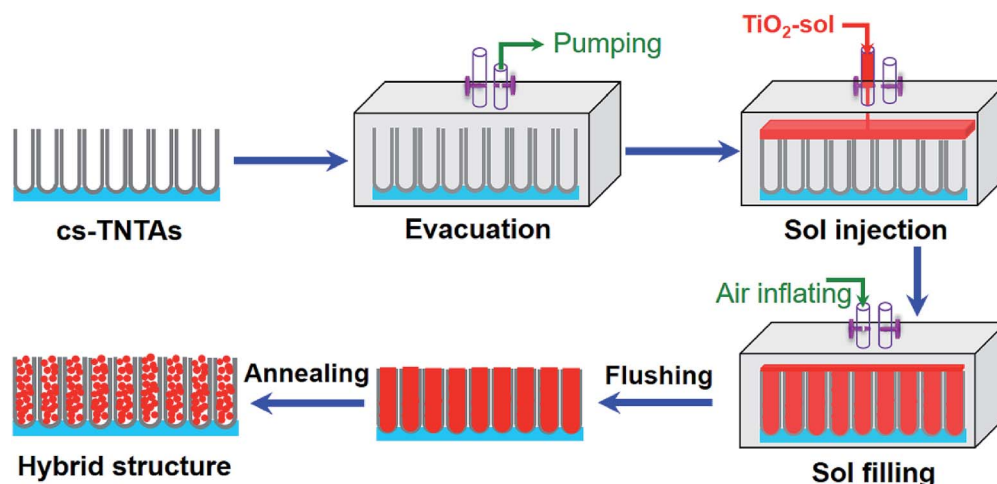


**Fig. 2** Schematic representation of the fabrication processes of the cigar-like hybrid structure through the vacuum-assisted filling technique, including evacuation, polymer contained  $\text{TiO}_2$ -sol injection, air inflating, surface flushing and annealing of the electrode at  $500^\circ\text{C}$ .

radical capturing.<sup>9,22,41</sup> The greatly reduced number of the carbonaceous heterogeneous nuclei can enable large grains during TNTA sintering.<sup>22</sup> The current transients recorded during the anodizing (at 50 V) (Fig. S6†) show a continuous increase in current density with the decrease of water content in the EG/DMSO based electrolyte, which is similar to that of TNTA growth in EG based solution.<sup>42,43</sup> A severe anodic etching of the Ti substrate and a more vigorous hydrogen evolution at the Pt cathode are observed when the water content is less than 1.5 vol%, due to the drastic anodization at large current density. Additionally, some carbon, which will induce heterogeneous nucleation as mentioned above, also appears in the TNTAs obtained under violent anodization conditions ( $H_2O \leq 1.5$  vol%, XRD in Fig. S7†), even when an EG/DMSO electrolyte is applied. The FTIR spectra (Fig. S8†) reveal that the as-prepared TNTAs derived from the EG/DMSO electrolyte with a moderate water content (1.8 vol%) contain the lowest amount of oxyhydroxide due to the low  $OH^-$  concentration in the electrolyte (see more explanation in the ESI†). The dehydroxylation of the amorphous  $TiO_x$  during annealing is identified as the initiation of the  $TiO_2$  crystallization process.<sup>24,44</sup> Therefore, a larger quantity of oxyhydroxide in the as-formed TNTAs will result in a larger number of crystal nuclei and thus a small grain size of nanotubes after sintering. The XRD patterns (Fig. S7†) of the as-prepared TNTAs indicate that  $TiO_x$  derived from the EG/DMSO electrolyte with  $H_2O$  less than 1.8 vol% remains almost amorphous, which is also evidenced by the weak and diffuse Raman response (Fig. S9†). The numerous partially crystallized sites can act as crystal nucleation sites for crystal growth during post-sintering. Therefore, it can be concluded here that the as-anodized TNTA films (derived from the EG/DMSO based electrolyte with a reasonably low  $H_2O$  content) with less carbon (or carbon free), less oxyhydroxide, and an amorphous structure are the key factors that result in the large columnar crystals during the post-annealing process (TEM images in Fig. S10†), as schematically shown in Fig. S11.† Further systematic studies on the role of the film composition, crystalline nature, wall thickness, and annealing process on the crystallization behavior of TNTAs are going on in our group with the aim to gain anodized nanotubes composed of even larger grains.

After the removal of any electrolyte residues and impurities in TNTAs by piranha solution soaking, the refined cs-TNTAs were then filled with mesoporous  $TiO_2$  networks to boost the surface area, *via* a vacuum-assisted sol filling approach schematically represented in Fig. 2. The filling procedures include the main steps of evacuation, polymer-contained  $TiO_2$ -sol injection, and air inflating (sol filling). To get a uniform  $TiO_2$ -sol filling into the whole nanotubes, it is very important to remove any air from the TNTAs beforehand since the air bubbles captured in the nanotube pores will hamper the filling of the viscous tri-block polymer F68 contained  $TiO_2$ -sol (Fig. 3 and S12†). After the  $TiO_2$ -sol injection and air-refilling, the  $TiO_2$ -sol easily fills into the evacuated pores of TNTAs under a pressure gradient. The as-prepared cs-TNTAs show an inner diameter of around 145 nm with a wall thickness of about 26 nm (Fig. 3a). In every filling, the cs-TNTA walls were uniformly decorated with a mesoporous  $TiO_2$  nanoparticle layer. No sharp interface can

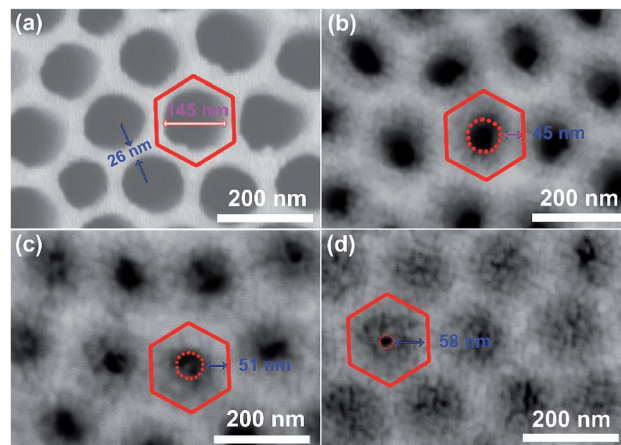


Fig. 3 SEM images showing the morphology evolution after repeated vacuum-assisted  $TiO_2$ -filling processes. (a) Pristine cs-TNTAs. (b–d) Nanoparticle/cs-TNTA hybrid structures after 1, 2 and 3 times of  $TiO_2$ -filling processes, respectively.

be observed between layers (Fig. 3b–d). After three times of filling, a “cigar-like”  $TiO_2$  nanoparticle/nanotube hybrid architecture was finally achieved (Fig. 3d). Further sol filling is not able to increase the  $TiO_2$  loading anymore, since the pores of the nanotube are already filled up with 3 times of filling (before 500 °C annealing). It is important to note that the block polymer, F68, has a strong effect on altering the morphology of the decorated  $TiO_2$  layer from an almost compact layer (without F68 inclusions, Fig. S13†) to a mesoporous network morphology (Fig. 3 and 4 discussed later). This is because the block polymer acts as a template and induces the self-assembly of the homogeneous  $TiO_2$  mesoporous networks.<sup>45,46</sup> TEM images (Fig. 4a and b) indicate that the  $TiO_2$  nanoparticles are firstly decorated along the entire wall surface (1 filling) and then extended into the whole inner space of nanotubes to a form a “cigar-like” hybrid architecture (3 times filling). The samples treated by 1, 2, 3 and 4 times of filling (cs-TNTAs- $x$ ,  $x = 1, 2, 3, 4$ ) are denoted, hereafter, as cs-TNTAs-1, cs-TNTAs-2, cs-TNTAs-3, and cs-TNTAs-4 respectively. TEM images of the top and bottom of cs-TNTAs-3 (Fig. 4d and e) illustrate a uniform filling throughout the whole nanotubes with  $TiO_2$  networks. The decorated  $TiO_2$  nanoparticles form a continuous and mesoporous network (Fig. 4f), where the small anatase  $TiO_2$  nanoparticles ( $\sim 15$  nm) are connected to each other. The XRD patterns (Fig. S14†) indicate the anatase nature of the  $TiO_2$  network for all samples. Due to the one-pot crystallization of amorphous cs-TNTAs- $x$  and the  $TiO_2$ -sol network, the nanoparticles are welded well with the nanotube wall to form a structure with good integrity (Fig. 4c). This mesoporous networks welded directly onto the nanotube wall will provide not only sufficient surface area for abundant dye-anchoring and a porous structure for unhampered dye and electrolyte penetration, but also an unhindered path for fast electron transfer (from networks into TNTAs) and reduced charge recombination.<sup>45–47</sup>

The active surface areas of the films available for N719 dye loading were estimated by a dye adsorption–desorption

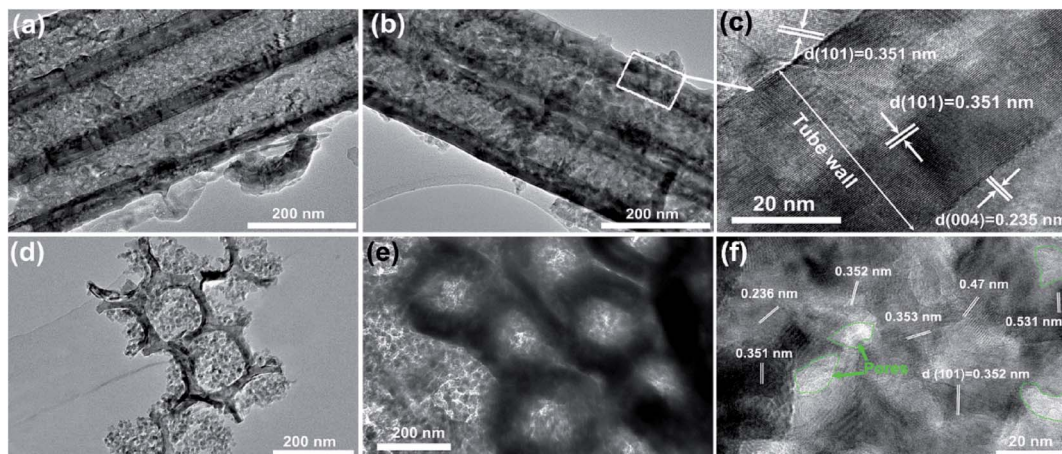


Fig. 4 TEM images of the nanoparticle/cs-TNTA hybrid structures. (a) and (b) Typical hybrid architectures after 1 and 3 times of filling processes, respectively. (c) HR-TEM image illustrating the welded structure of the cs-TNTA wall and the decorated TiO<sub>2</sub> nanoparticles. (d) and (e) Top and bottom, respectively, of nanoparticle/cs-TNTAs after 3 times of filling, showing the uniform filling of TiO<sub>2</sub> nanoparticles into the entire nanotubes. (f) HR-TEM image illustrating the mesoporous network of the TiO<sub>2</sub> nanoparticle layers.

technique.<sup>46</sup> The film thickness was carefully controlled at around  $18 \pm 0.15 \mu\text{m}$  for all samples. The free-standing cs-TNTA films, which were firstly characterized by the nitrogen adsorption-desorption technique, were used as a standard control. The BET specific surface area of the cs-TNTAs is measured to be  $21.3 \text{ m}^2 \text{ g}^{-1}$ . The relative surface roughness factor of the pristine

cs-TNTAs is thus calculated to be 24.9-fold per  $\mu\text{m}$  thickness of the film, according to the BET surface area and mass of the film. According to the UV-Vis absorption measurements (Fig. 5a, S15<sup>†</sup>), the N719 dye-loading amounts are calculated to be  $0.91 \times 10^{-7}$ ,  $2.12 \times 10^{-7}$ ,  $2.91 \times 10^{-7}$ , and  $3.43 \times 10^{-7} \text{ mol cm}^{-2}$  for bare cs-TNTAs, cs-TNTAs-1, cs-TNTAs-2, and cs-TNTAs-3,

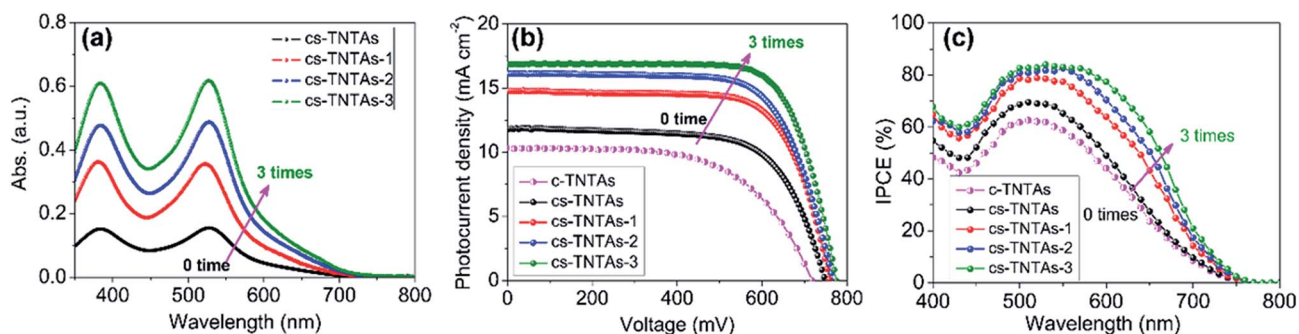


Fig. 5 (a) UV-vis spectra of the N719 dye solution desorbed from the nanoparticle/cs-TNTA hybrid with 0, 1, 2, and 3 times of TiO<sub>2</sub> filling. (b) Photocurrent density-photovoltage ( $J$ - $V$ ) curves of front-illuminated DSSCs measured under  $100 \text{ mW cm}^{-2}$  illumination and (c) IPCE spectra of DSSCs based on various photoanodes employing the nanoparticle/cs-TNTA hybrid with 0, 1, 2, and 3 times of TiO<sub>2</sub> filling.

Table 1 Photovoltaic parameters of the nanoparticle/cs-TNTA hybrid structure based DSSCs, measured under  $100 \text{ mW cm}^{-2}$  of front-illumination<sup>a</sup>

Devices	$J_{sc}$ [ $\text{mA m}^{-2}$ ]	$V_{oc}$ [V]	FF	PCE [%]	Dye-loading [ $\times 10^{-7} \text{ mol cm}^{-2}$ ]
c-TNTAs	$10.33 \pm 0.35$	$0.72 \pm 0.01$	$0.61 \pm 0.02$	$4.54 \pm 0.35$	$0.97 \pm 0.03$
cs-TNTAs	$11.84 \pm 0.15$	$0.75 \pm 0.005$	$0.62 \pm 0.01$	$5.51 \pm 0.15$	$0.91 \pm 0.02$
cs-TNTAs-1	$14.92 \pm 0.25$	$0.76 \pm 0.001$	$0.67 \pm 0.01$	$7.60 \pm 0.25$	$2.12 \pm 0.03$
cs-TNTAs-2	$16.19 \pm 0.25$	$0.76 \pm 0.007$	$0.68 \pm 0.01$	$8.37 \pm 0.25$	$2.91 \pm 0.03$
cs-TNTAs-3	$16.87 \pm 0.15$	$0.77 \pm 0.005$	$0.69 \pm 0.01$	$8.96 \pm 0.15$	$3.43 \pm 0.02$
cs-TNTAs-4	$16.79 \pm 0.20$	$0.77 \pm 0.007$	$0.69 \pm 0.02$	$8.87 \pm 0.25$	$3.45 \pm 0.02$

<sup>a</sup> The photovoltaics are taken from at least 7 devices.

Table 2 Electrochemical parameters extracted from the electrochemical impedance spectroscopy results

Devices	$R_w$ [ $\Omega$ ]	$R_k$ [ $\Omega$ ]	$k_{\text{eff}}$ [ $\text{s}^{-1}$ ]	$\tau_c$ [ms]	$D_{\text{eff}}$ [ $\times 10^{-4} \text{ cm}^2 \text{ s}^{-1}$ ]	$\eta_{\text{cc}}$ [%]	$L_n$ [ $\mu\text{m}$ ]
c-TNTAs	2.59	21.2	15.8	63	4.26	88	52
cs-TNTAs	1.02	35.7	5	200	5.66	97.1	106
cs-TNTAs-1	0.84	33.2	6.28	159	8.04	97.5	113
cs-TNTAs-2	0.7	31.4	6.97	143	10.1	97.7	120
cs-TNTAs-3	0.63	28.4	7.52	134	10.9	97.8	121

respectively. Assuming the same dye loading mechanism for all the samples and all the measured BET surface area is accessible for the N719 adsorption ( $\sim 1.6 \text{ nm}^2$  per N719 molecule), the accessible surface roughness is estimated to be 56.8-, 78.4-, and 93.3-fold per  $\mu\text{m}$  thickness of the film for cs-TNTAs-1, cs-TNTAs-2, and cs-TNTAs-3, respectively. This remarkably increased active surface area and dye-loading capacity will enable sensitized photoanodes with high light-harvesting efficiency.

The hybrid structures with a film thickness of  $18 \pm 0.15 \mu\text{m}$  were exploited as photoanodes for front-illuminated DSSCs. The c-TNTA based solar cell shows a low power conversion efficiency (PCE) of 4.54% (Fig. 5b and Table 1). In contrast, a much higher PEC of 5.51% is achieved for the bare cs-TNTA based device, with a remarkable improvement in all photovoltaic parameters, namely short-circuit current density ( $J_{\text{sc}}$ ), open-circuit voltage ( $V_{\text{oc}}$ ) and fill factor (FF), compared with the c-TNTA based cells. As the  $\text{TiO}_2$  filling increases from 1 to 3 times, the  $J_{\text{sc}}$  gains a significant improvement for hybrid architecture based DSSCs. A maximum efficiency of 8.96% is achieved for the cs-TNTAs-3 based device. This PCE is 163% and 197% that of bare cs-TNTAs and c-TNTA based devices, respectively. The cs-TNTAs-4 shows a similar photovoltaic performance to cs-TNTAs-3, since the 4<sup>th</sup>  $\text{TiO}_2$ -sol filling cannot increase the thickness of the decorated  $\text{TiO}_2$  layer and thus the dye-loading amount of the photoanode, as mentioned before. A comparison of the photovoltaics also witnesses a sustained increase in  $V_{\text{oc}}$  values from 0.75 V for the pristine cs-TNTA based DSSC to 0.77 V for the cs-TNTAs-3 based one, which might be ascribed to the increased quasi-Fermi level of the  $\text{TiO}_2$  film with increased electron density under illumination. For the DSSCs employing c-TNTA based hybrid structures obtained by the same vacuum-assisted sol-filling approach, however, both the PCE and  $V_{\text{oc}}$  suffer a continuous decline after the first  $\text{TiO}_2$  filling (Table S1†). We speculate that the hampered electron transport/transfer and thus increased charge recombination at the nanotube inner wall/particle interface deteriorate the performance.

It can be seen from the incident photon to current conversion efficiency (IPCE) spectra (Fig. 5c) that the cs-TNTA based DSSCs exhibit greater IPCE over the whole investigated wavelength zone than the c-TNTA based device. By filling cs-TNTAs with  $\text{TiO}_2$  networks, the DSSCs yield further IPCE enhancement over the entire wavelength region. It is clear that the IPCE becomes more pronounced in the longer wavelength zone as the  $\text{TiO}_2$  filling increased, indicating excellent photocurrent responses in the lower photon energy range for the cs-TNTAs- $x$  based solar cells. As the N719 dye shows remarkably lower light

extinction capacity for long wavelength light, the many multiples of increased dye loading will facilitate the light harvesting in this zone and boost the  $J_{\text{sc}}$  and PCE of the resulting DSSCs.

As shown in Table 1, the dye loading of cs-TNTAs is slightly lower than that of c-TNTAs ( $0.91 \times 10^{-7}$  vs.  $0.97 \times 10^{-7} \text{ mol cm}^{-2}$ ), due to the relatively smooth surface of columnar single-crystal based nanotube walls, suggesting that the improved charge collection rather than light harvesting contributes to the improved PCE of the cs-TNTA based device. The Hall-effect measurements reveal a higher electron mobility of  $3.14 \text{ cm}^2 \text{ V}^{-1} \text{ s}^{-1}$  at room temperature ( $30^\circ \text{C}$ ) for cs-TNTAs while this value is  $0.62 \text{ cm}^2 \text{ V}^{-1} \text{ s}^{-1}$  for c-TNTAs (Table S2†). The resistivity test also demonstrated around two orders of magnitude higher conductivity of the cs-TNTA film in comparison with c-TNTAs (Fig. S16†). Electrochemical impedance spectroscopy (EIS) measurements were conducted to investigate the electron transport behaviors of devices with various photoanodes. The concerned parameters are extracted by fitting the EIS results

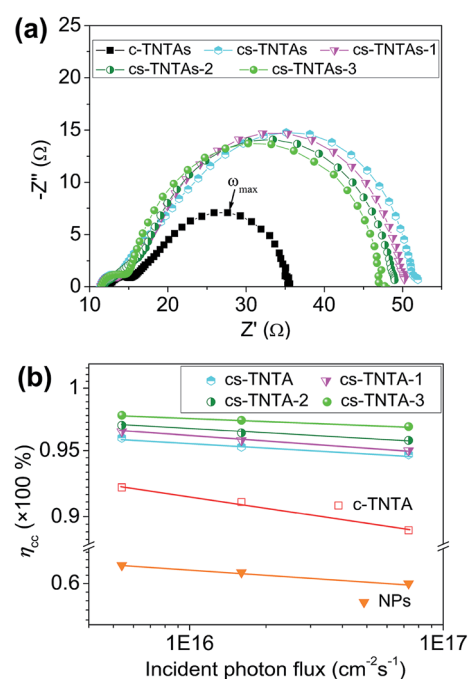


Fig. 6 (a) Nyquist plots of the c-TNTA, cs-TNTA, and cs-TNTAs- $x$  ( $x = 1, 2, 3$ ) based DSSCs measured under open-circuit conditions under  $100 \text{ mW cm}^{-2}$  illumination, (b) charge collection efficiency  $\eta_{\text{cc}}$  of the c-TNTA, nanoparticle (NP) film, and cs-TNTAs- $x$  ( $x = 0, 1, 2, 3$ ) based DSSCs as a function of incident photo flux.

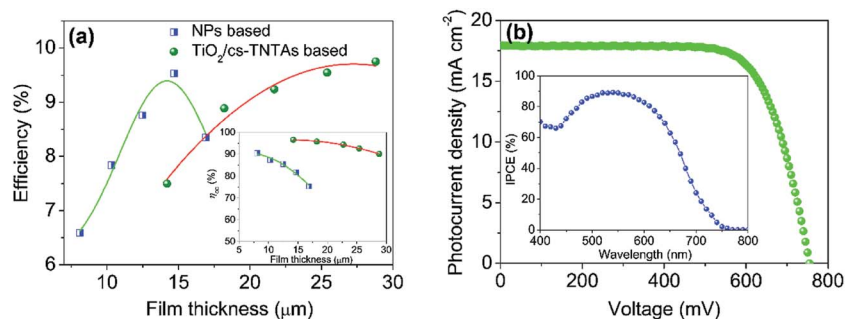


Fig. 7 (a) Power conversion efficiency and charge collection efficiency (inset) of TiO<sub>2</sub>/cs-TNTA and NP-based DSSCs as a function of film thickness of photoanodes. (b) Photocurrent density–photovoltage ( $J$ - $V$ ) curve and IPCE spectrum (inset) of the champion DSSCs based on a TiO<sub>2</sub>/cs-TNTA photoanode with a film thickness of around 28.8 μm.

according to the equivalent circuits represented by a transmission line model (inset of Fig. S17†).<sup>48–51</sup> From the fitted data, we could calculate the parameters such as the electron lifetime  $\tau_e = (2\pi f_{\max})^{-1}$  ( $f_{\max}$  is the peak frequency corresponding to the second arc in the Nyquist plots in the case of  $R_k \gg R_w$ ), the recombination rate  $k_{\text{eff}} = 2\pi f_{\max}$ , the charge collection efficiency  $\eta_{\text{cc}} = 1 - R_w/R_k$ , the electron diffusion coefficient  $D_{\text{eff}} = (R_k/R_w)L^2k_{\text{eff}}$ , and the theoretical effective diffusion length  $L_n = (D_{\text{eff}}\tau_e)^{1/2}$ .<sup>49–51</sup> It is clear from Table 2 that the cs-TNTA based device possesses 2.5 times less electron transport resistance ( $R_w = r_wL$ ) (1.02 Ω vs. 2.59 Ω) while the recombination rate is 3 times lower than that of c-TNTAs due to the higher electron mobility and fewer grain boundaries in the columnar crystal based nanotube walls. As a result, the cs-TNTA based device delivers a significantly higher  $\eta_{\text{cc}}$  (97.1% vs. 88%) than c-TNTA based cells. The  $L_n$  of cs-TNTAs is as long as 106 μm which is double that of c-TNTAs (52 μm), implying that the cs-TNTA film can be made thicker than c-TNTA counterparts and thus allows for a higher light harvesting. The prominent charge collection is responsible, as expected, for the improved performance of cs-TNTA based DSSCs. As the TiO<sub>2</sub> filling increased from 0 to 3 times, the recombination rate,  $k_{\text{eff}}$ , increased slightly because of the increased dye/electrolyte interface while the  $R_w$  kept on decreasing due to the enhanced conductivity of TiO<sub>2</sub> with more photoelectron injection. Interestingly, no  $\eta_{\text{cc}}$  decline but a slight improvement is observed for the cs-TNTAs- $x$  ( $x = 1, 2, 3$ ) based DSSCs upon the TiO<sub>2</sub> filling increment, suggesting that the electron transport mechanism is not affected by thickening the TiO<sub>2</sub> network. Additionally, the  $\eta_{\text{cc}}$  decreases only slightly with increasing incident light intensity (Fig. 6b), indicating the excellent capacity of the developed hierarchical photoanodes to efficiently collect electrons with different charge concentrations. In contrast, increasing the thickness of TiO<sub>2</sub> decoration or increasing light intensity degrades the  $\eta_{\text{cc}}$  remarkably for the devices based on c-TNTA based hybrids (Table S1,† Fig. 6b) due to the increased recombination under the competitive electron transport mechanism (fast through TNTAs and slow through the TiO<sub>2</sub> network), similar to reported work,<sup>30</sup> as sketched in Scheme 1. The significant decrease of  $V_{\text{oc}}$  values (Table S1†) is in line with this increased recombination in c-TNTAs- $x$ . The Hall-effect measurements

confirm a significantly larger electron mobility difference between cs-TNTAs and the TiO<sub>2</sub> network (3.14 vs. 0.43 cm<sup>2</sup> V<sup>-1</sup> s<sup>-1</sup>) than that between c-TNTAs and the TiO<sub>2</sub> network (0.62 vs. 0.43 cm<sup>2</sup> V<sup>-1</sup> s<sup>-1</sup>). Based on the EIS and Hall-effect results, it is reasonable to conclude that an electrically heterogeneous hybrid is formed in the welded TiO<sub>2</sub>-network/cs-TNTA hierarchical structure, where the cs-TNTAs with high electron mobility, high conductivity, and long diffusion length effectively drain the photogenerated electrons from the TiO<sub>2</sub> network and transport them quickly along the well-aligned nanotube walls, as schematically represented in Scheme 1, leading to the prominently high  $\eta_{\text{cc}}$  and impressive efficiency of the developed DSSCs.

As the obtained cs-TNTAs-3 device shows a much longer theoretical effective diffusion length,  $L_n$ , than the real film thickness employed (121 vs. 18 μm), the thickness of active films, which is of key importance to the dye-loading capacity and thus the light-harvesting of the solar cells, is increased to further boost the PCE of cs-TNTAs-3 based DSSCs. The dye adsorption amount of cs-TNTAs-3 based photoanodes increases almost linearly with increasing film thickness (Fig. S18†). In contrast to the remarkably decreased  $\eta_{\text{cc}}$  due to increased TiO<sub>2</sub> film thickness for the NP-based device, cs-TNTAs-3 based DSSCs retain a high electron collection capacity over 90% even with a film thickness up to about 30 μm (inset of Fig. 7a). By carefully controlling of the growth conditions, cs-TNTAs up to 28.8 μm were finally obtained to construct the “cigar-like” architecture for DSSCs. The resulting solar cells exhibit a  $J_{\text{sc}}$  of 18.05 mA cm<sup>-2</sup>, a  $V_{\text{oc}}$  of 0.76 V and an FF of 0.73. As a result, an impressively high PCE of 10.1% was achieved, which is even slightly higher than that of the optimized NP-based DSSCs with an efficiency of 9.63% (Fig. S19†). We believe that an even greater efficiency could be achieved, if thicker cs-TNTAs can be fabricated with an improved technique or if the N719 dye can be replaced by other absorbers with broadened and stronger absorption (such as ADEKA-1, Y123, YD2-o-C8 or their cocktail forms).<sup>1,2,52</sup>

### 3. Conclusion

In the presented work, long columnar-single-crystal based TNTAs which feature a single-wall morphology and improved electron mobility were successfully developed. Combined with

a newly proposed vacuum-assisted TiO<sub>2</sub>-sol filling approach, hierarchical cs-TNTA architectures were obtained for DSSCs. The decorated TiO<sub>2</sub> network is firmly welded to the nanotube wall and possessed a mesoporous feature, providing a vast surface area for dye loading. The significant mismatch in electron mobility between the cs-TNTA scaffold and mesoporous TiO<sub>2</sub>-network decoration drives the electron flow from the TiO<sub>2</sub> network to the cs-TNTAs, enabling fast electron transport and enhancing charge collection efficiency. An impressively high PEC of up to 10.1% was achieved for the resulting DSSCs due to the balanced high dye loading and excellent charge collection capacity. The developed TiO<sub>2</sub> nanotubes with columnar crystals and their derived hybrid structures should also be attractive for other applications, such as photocatalysis, photosynthesis, photoelectrochemical reactions, and so on.

## 4. Experimental section

### 4.1 Preparation of c-TNTAs and cs-TNTAs

TiO<sub>2</sub> nanotube arrays (TNTAs) were prepared by a two-step electrochemical anodization technique similar to our previous work.<sup>18</sup> For the fabrication of well-aligned and long columnar-crystal based TNTAs (cs-TNTAs), the classical EG based electrolyte was replaced by a mixed solvent electrolyte composed of 0.4 wt% NH<sub>4</sub>F (≥99.99% trace metals basis, Sigma-Aldrich) and various H<sub>2</sub>O contents (*i.e.* 3.0, 1.8, 1.5, 0.5 vol%) in EG/DMSO (1 : 1 vol%). To carefully control the water content in the electrolyte, any moisture in EG (anhydrous, 99.8%, Sigma-Aldrich) was removed through a molecular sieve column (Linde4A) before use. It's noteworthy that, because of the highly hygroscopic nature of EG and NH<sub>4</sub>F, ultrapure reagents should be used and handled in a N<sub>2</sub> atmosphere. The anodization was carried out using a sealed two-electrode cell to avoid moisture absorption and the electrolyte was controlled at 20 °C by using a cooling system. The anodization was conducted at 50 V for 2–5 h to achieve cs-TNTAs with desired thickness. Conventional TNTAs (c-TNTAs) were also prepared at 50 V for 2–3 h in an open system for reference, using the classical electrolyte containing NH<sub>4</sub>F (0.4 wt%) in EG (3 vol%).<sup>18</sup>

### 4.2 Preparation of TiO<sub>2</sub> sol

The TiO<sub>2</sub> sol was prepared according to our previous work but with modification.<sup>48</sup> In short, acetic acid (25 mL) was added to distilled water (50 mL) and then cooled in an ice-water bath for 2 h. Titanium(IV) isopropoxide (7 mL) was first mixed with isopropanol (15 mL) and then added dropwise to the above acetic acid solution under vigorous stirring. The mixture was placed in an ice-water bath and kept stirring overnight. Subsequently, the mixture was heated to 80 °C in an oil bath to evaporate isopropanol and a portion of acetic acid under violent stirring till a light-blue sol was obtained. For the polymer (F68, poly(ethylene glycol)-*block*-poly(propylene glycol)-*block*-poly(ethylene glycol)) containing sol, a certain amount of F68 powder (2 : 1 ratio with respect to TiO<sub>2</sub> solid content, wt%) was dispersed in the obtained TiO<sub>2</sub>-sol by vigorous stirring. The sol was aged for at least 2 days in a 4 °C fridge before use.

### 4.3 Preparation of hierarchical structures

The filling of TiO<sub>2</sub> sol into the TNTAs was realized by a vacuum-assisted filling approach, employing a home-made vacuum chamber. Prior to filling, the cs-TNTAs were annealed at 150 °C for 30 minutes, followed by casting drops of piranha solution (H<sub>2</sub>SO<sub>4</sub> : H<sub>2</sub>O<sub>2</sub> (30%), 7 : 3) on the cs-TNTA electrodes to remove any contaminants (stayed for 5–10 s dependent on the film thickness) and achieve a clean nanotube wall surface (**Caution:** piranha solution reacts violently with organic chemicals). The etched electrodes were carefully washed with plenty of ethanol to remove any piranha residue in the nanotubes. For TiO<sub>2</sub>-sol filling, the cs-TNTAs were put into a vacuum chamber and evacuated to around 5 mbar by using an oil pump (GVD 1.5). The pressure was kept for 5 minutes, followed by injection of the TiO<sub>2</sub>-sol into the vessel. After that, the gas was refilled into the chamber slowly and the TiO<sub>2</sub>-sol was forced into the TNTAs under a pressure gradient. The electrodes were flushed carefully with ethanol to remove any sol left on the top surface of the electrodes and dried at 120 °C for 10 minutes to evaporate solvent before another sol-filling process. The electrodes treated with 0, 1, 2, 3 and 4 times of sol-filling were subjected to 2 h sintering at 500 °C with a ramp rate of 1 °C min<sup>-1</sup> for the crystallization of TiO<sub>2</sub>.

### 4.4 Fabrication of DSSCs

The TiO<sub>2</sub> films were peeled off from the Ti substrates by a third anodization, followed by a H<sub>2</sub>O<sub>2</sub> solution soaking, according to previous work.<sup>18,28</sup> The closed bottoms of TNTAs were removed by a mechanical grinding approach described in our previous work.<sup>53</sup> The obtained free-standing open-ended TNTA films were transferred onto ITO glass employing our reported method to complete the fabrication of photoanodes.<sup>18</sup> Various photoanodes were sensitized in a N719 ethanol solution (0.5 M) overnight and then assembled into DSSCs with a sputtered Pt counter electrode and a liquid electrolyte composed of LiI (0.5 M), I<sub>2</sub> (0.05 M), 1-methyl-3-hexylimidazolium iodide (HMII, 0.3 M), *N*-methylbenzimidazole (NMB, 0.3 M), and 4-*tert*-butylpyridine (0.5 M) in 3-ethoxypropionitrile.

### 4.5 Measurements and characterization

The structure and morphology of the TNTAs and hybrids were observed by a field-emission scanning electron microscope (Hitachi S-4800) and a high-resolution transmission electron microscope (TEM, JEM 2011, Japan; 200 kV). The crystal structure was identified by using X-ray diffraction (XRD, Rigaku 9 kW SmartLab, Japan) patterns. The dye-loading amount was evaluated by using a UV-Vis spectrophotometer (Model UV-2550, Shimadzu, Japan). *I*-*V* characteristic curves of DSSCs with an active area of 0.16 cm<sup>-2</sup> were recorded using a Keithley 2420 source meter under AM 1.5 G illumination (100 mW cm<sup>-2</sup>) supplied by a 300 W solar simulator (Model 69911, Newport-Oriel Instruments, USA). The illumination intensity was calibrated using a silicon reference cell (NIST) equipped with a power meter. The IPCE was tested by using a Newport 2931-C system equipped with a Newport 74125 monochromator. The

light source was provided by a Newport 66902 solar simulator. Electrochemical impedance spectroscopy (EIS) was performed under  $100 \text{ mW cm}^{-2}$  of AM 1.5 illumination in an open-circuit situation, using a Solartron 1255B frequency response analyzer and a Solartron SI 1287 electrochemical interface system. The frequency range was 100 kHz to 0.1 Hz. The intensity modulated photocurrent spectroscopy (IMPS) and intensity modulated photovoltage spectroscopy (IMVS) measurements were performed using a green light emitting diode (LED, peak wavelength 520 nm) driven by a Solartron 1255B frequency-response analyzer.

## Conflicts of interest

There are no conflicts to declare.

## Acknowledgements

This work was financially supported by the National Natural Science Foundation of China (Grants No. 61604058, 51673204, and 51602010), the Fundamental Research Funds for the Central Universities (2017MS003), the Research Grants Council of the Hong Kong Special Administrative Region, China (Project No. PolyU152057/14E), the Hong Kong Polytechnic University (Project No. 1-ZVGH), and National Materials Genome Project (2016YFB0700600).

## References

- 1 K. Kakiage, Y. Aoyama, T. Yano, K. Oya, J. I. Fujisawa and M. Hanaya, *Chem. Commun.*, 2015, **51**, 15894–15897.
- 2 Y. Cao, Y. Liu, S. M. Zakeeruddin, A. Hagfeldt and M. Grätzel, *Joule*, 2018, **2**, 1108–1117.
- 3 X. Meng, C. Yu, X. Song, J. Iocozzia, J. Hong, M. Rager, H. Jin, S. Wang, L. Huang, J. Qiu and Z. Lin, *Angew. Chem., Int. Ed.*, 2018, **57**, 4682–4686.
- 4 D. H. Kweon and J. B. Baek, *Adv. Mater.*, 2019, **31**, 1804440.
- 5 X. Meng, C. Yu, X. Zhang, L. Huang, M. Rager, J. Hong, J. Qiu and Z. Lin, *Nano Energy*, 2018, **54**, 138–147.
- 6 N. Fu, Y. Y. Fang, Y. D. Duan, X. W. Zhou, X. R. Xiao and Y. Lin, *ACS Nano*, 2012, **6**, 9596–9605.
- 7 X. Meng, C. Yu, X. Song, Y. Liu, S. Liang, Z. Liu, C. Hao and J. Qiu, *Adv. Energy Mater.*, 2015, **5**, 1500180.
- 8 X. Meng, C. Yu, X. Song, Z. Liu, B. Lu, C. Hao and J. Qiu, *J. Mater. Chem. A*, 2017, **5**, 2280–2287.
- 9 S. So, I. Hwang and P. Schmuki, *Energy Environ. Sci.*, 2015, **8**, 849–854.
- 10 K. Lee, A. Mazare and P. Schmuki, *Chem. Rev.*, 2014, **114**, 9385–9454.
- 11 J. Tian, Z. Zhao, A. Kumar, R. I. Boughton and H. Liu, *Chem. Soc. Rev.*, 2014, **43**, 6920–6937.
- 12 S. So, I. Hwang, J. Yoo, S. Mohajernia, M. Mačkovič, E. Spiecker, G. Cha, A. Mazare and P. Schmuki, *Adv. Energy Mater.*, 2018, **8**, 1800981.
- 13 W. Guo, C. Xu, X. Wang, S. Wang, C. Pan, C. Lin and Z. L. Wang, *J. Am. Chem. Soc.*, 2012, **134**, 4437–4441.
- 14 Y. H. Jang, X. Xin, M. Byun, Y. J. Jang, Z. Lin and D. H. Kim, *Nano Lett.*, 2012, **12**, 479–485.
- 15 C. T. Yip, H. Huang, L. Zhou, K. Xie, Y. Wang, T. Feng, J. Li and W. Y. Tam, *Adv. Mater.*, 2011, **23**, 5624–5628.
- 16 X. Xin, B. Li, J. Jung, Y. J. Yoon, R. Biswas and Z. Lin, *Part. Part. Syst. Charact.*, 2015, **32**, 80–90.
- 17 D. Zheng, X. Pang, M. Wang, Y. He, C. Lin and Z. Lin, *Chem. Mater.*, 2015, **27**, 5271–5278.
- 18 N. Fu, Y. Liu, Y. Liu, W. Lu, L. Zhou, F. Peng and H. Huang, *J. Mater. Chem. A*, 2015, **3**, 20366–20374.
- 19 M. Yang, D. Kim, H. Jha, K. Lee, J. Paul and P. Schmuki, *Chem. Commun.*, 2011, **47**, 2032–2034.
- 20 M. Ye, D. Zheng, M. Lv, C. Chen, C. Lin and Z. Lin, *Adv. Mater.*, 2013, **25**, 3039–3044.
- 21 A. Elzarka, N. Liu, I. Hwang, M. Kamal and P. Schmuki, *Chem.–Eur. J.*, 2017, **23**, 12995–12999.
- 22 H. Mirabolghasemi, N. Liu, K. Lee and P. Schmuki, *Chem. Commun.*, 2013, **49**, 2067–2069.
- 23 J. Lin, M. Guo, C. T. Yip, W. Lu, G. Zhang, X. Liu, L. Zhou, X. Chen and H. Huang, *Adv. Funct. Mater.*, 2013, **23**, 5952–5960.
- 24 S. Lee, I. J. Park, D. H. Kim, W. M. Seong, D. W. Kim, G. S. Han, J. Y. Kim, H. S. Jung and K. S. Hong, *Energy Environ. Sci.*, 2012, **5**, 7989–7995.
- 25 W.-C. Chen, M.-H. Yeh, L.-Y. Lin, R. Vittal and K.-C. Ho, *ACS Sustainable Chem. Eng.*, 2018, **6**, 3907–3915.
- 26 M. Guo, K. Xie, J. Lin, Z. Yong, C. T. Yip, L. Zhou, Y. Wang and H. Huang, *Energy Environ. Sci.*, 2012, **5**, 9881–9888.
- 27 J. S. Kang, H. Choi, J. Kim, H. Park, J.-Y. Kim, J.-W. Choi, S.-H. Yu, K. J. Lee, Y. S. Kang, S. H. Park, Y.-H. Cho, J.-H. Yum, D. C. Dunand, H. Choe and Y.-E. Sung, *Small*, 2017, **13**, 1701458.
- 28 N. Fu, X. Li, Y. Liu, Y. Liu, M. Guo, W. Li and H. Huang, *J. Power Sources*, 2017, **343**, 47–53.
- 29 J. Lin, X. Liu, M. Guo, W. Lu, G. Zhang, L. Zhou, X. Chen and H. Huang, *Nanoscale*, 2012, **4**, 5148–5153.
- 30 J. Choi, G. Kang and T. Park, *Chem. Mater.*, 2015, **27**, 1359–1366.
- 31 S. Kurian, P. Sudhagar, J. Lee, D. Song, W. Cho, S. Lee, Y. S. Kang and H. Jeon, *J. Mater. Chem. A*, 2013, **1**, 4370–4375.
- 32 M. Ye, X. Xin, C. Lin and Z. Lin, *Nano Lett.*, 2011, **11**, 3214–3220.
- 33 K. Zhu, N. R. Neale, A. Miedaner and A. J. Frank, *Nano Lett.*, 2007, **7**, 69–74.
- 34 J. E. Kroeze, T. J. Savenije and J. M. Warman, *J. Am. Chem. Soc.*, 2004, **126**, 7608–7618.
- 35 H. Tang, K. Prasad, R. Sanjinès, P. E. Schmid and F. Lévy, *J. Appl. Phys.*, 1994, **75**, 2042–2047.
- 36 L. Forro, O. Chauvet, D. Emin, L. Zuppiroli, H. Berger and F. Lévy, *J. Appl. Phys.*, 1994, **75**, 633–635.
- 37 S. So, I. Hwang, J. Yoo, S. Mohajernia, M. Mačkovič, E. Spiecker, G. Cha, A. Mazare and P. Schmuki, *Adv. Energy Mater.*, 2018, **8**, 1800981.
- 38 X. Feng, K. Shankar, O. K. Varghese, M. Paulose, T. J. Latempa and C. A. Grimes, *Nano Lett.*, 2008, **8**, 3781–3786.